ARL

US Army Research Laboratory

Computational Fluid Dynamics (CFD) Simulations of a Finned Projectile with Microflaps for Flow Control

by Jubaraj Sahu

NOTICES

Disclaimers

The findings in this report are not to be construed as an official Department of the Army position unless so designated by other authorized documents.

Citation of manufacturer's or trade names does not constitute an official endorsement or approval of the use thereof.

Destroy this report when it is no longer needed. Do not return it to the originator.

US Army Research Laboratory

Computational Fluid Dynamics (CFD) Simulations of a Finned Projectile with Microflaps for Flow Control

by Jubaraj Sahu
Weapons and Materials Research Directorate, ARL

REPORT DOCUMENTATION PAGE			Form Approved OMB No. 0704-0188

Public reporting burden for this collection of information is estimated to average 1 hour per response, including the time for reviewing instructions, searching existing data sources, gathering and maintaining the data needed, and completing and reviewing the collection of information. Send comments regarding this burden estimate or any other aspect of this collection of information, including suggestions for reducing the burden, to Department of Defense, Washington Headquarters Services, Directorate for Information Operations and Reports (0704-0188), 1215 Jefferson Davis Highway, Suite 1204, Arlington, VA 22202-4302. Respondents should be aware that notwithstanding any other provision of law, no person shall be subject to any penalty for failing to comply with a collection of information if it does not display a currently valid OMB control number.
PLEASE DO NOT RETURN YOUR FORM TO THE ABOVE ADDRESS.

1. REPORT DATE *(DD-MM-YYYY)*	2. REPORT TYPE	3. DATES COVERED (From - To)
April 2016	Final	October 2014–July 2015

4. TITLE AND SUBTITLE	5a. CONTRACT NUMBER
Computational Fluid Dynamics (CFD) Simulations of a Finned Projectile with Microflaps for Flow Control	
	5b. GRANT NUMBER
	5c. PROGRAM ELEMENT NUMBER
6. AUTHOR(S)	5d. PROJECT NUMBER
Jubaraj Sahu	AH80
	5e. TASK NUMBER
	5f. WORK UNIT NUMBER

7. PERFORMING ORGANIZATION NAME(S) AND ADDRESS(ES)	8. PERFORMING ORGANIZATION REPORT NUMBER
US Army Research Laboratory ATTN: RDRL-WML-E Aberdeen Proving Ground, MD 21005-5066	ARL-TR-7660

9. SPONSORING/MONITORING AGENCY NAME(S) AND ADDRESS(ES)	10. SPONSOR/MONITOR'S ACRONYM(S)
	11. SPONSOR/MONITOR'S REPORT NUMBER(S)

12. DISTRIBUTION/AVAILABILITY STATEMENT
Approved for public release; distribution is unlimited.

13. SUPPLEMENTARY NOTES

14. ABSTRACT
This research describes a computational study undertaken to determine the effect of a flow control mechanism and its associated aerodynamics for a finned projectile. The flow control system consists of small microflaps located between the rear fins of the projectile. These microflaps alter the flow field in the finned region of the projectile, resulting in asymmetric pressure distribution and thus producing control forces and moments. A number of different geometric parameters, microflap locations, and the number of microflaps were varied in an attempt to maximize the control authority generated by the flaps. Steady-state Navier-Stokes computations were performed to obtain the control aerodynamic forces and moments associated with the microflaps. These results were used to optimize the control authority at a supersonic speed, M = 2.5. Computed results not only showed the microflaps to be effective at this speed, but also 6 and 8 microflaps were found to generate 25%–50% more control force than a baseline 4-flap configuration. These results led to a new optimized 8-flap configuration that was further investigated for a range of Mach numbers from M = 0.8 to 5.0 and was found to be a viable configuration effective in providing control at all of these speeds.

15. SUBJECT TERMS
flow control, finned projectile, CFD applications, microflaps, optimized control force

16. SECURITY CLASSIFICATION OF:			17. LIMITATION OF ABSTRACT	18. NUMBER OF PAGES	19a. NAME OF RESPONSIBLE PERSON
					Jubaraj Sahu
a. REPORT	b. ABSTRACT	c. THIS PAGE	UU	32	19b. TELEPHONE NUMBER (Include area code)
Unclassified	Unclassified	Unclassified			410-306-0798

Standard Form 298 (Rev. 8/98)
Prescribed by ANSI Std. Z39.18

ii

Contents

List of Figures

List of Tables

Acknowledgments

1.   Introduction

Accurate determination of aerodynamics and flight dynamics is critical to the low-cost development of new advanced guided projectiles and missiles. For a guided munition, control force and moment must be generated by some means to alter its trajectory as needed. Traditionally, fins, canards, and jets have been used to provide control for maneuvering projectiles and missiles. The flow fields associated with these control mechanisms for US Army weapons are complex, involving 3-dimensional (3-D) shock-boundary layer interactions, jet interaction with the free stream flow, and highly viscous–dominated separated flow regions.[1–3] Recently, many new weapon control mechanisms such as deployable pins,[4,5] microflaps,[6–8] and microjets[9–12] have been investigated for their feasility for providing sufficient control forces and moments for projectile control. The effect of these new flow control mechanisms on flight dynamics of munitions is again critical to overall guided flight performance. Many of these mechanisms fall outside the range of conventional aerodynamic control, and accurate prediction of aerodynamic loads is desired. These control mechanisms result in highly complex unsteady flow interactions, and their accurate modeling during guided flight with active control is a major challenge both in terms of time-accurate solution techniques and computing resources required. Fortunately, improved computer technology and state-of-the-art numerical procedures now enable solutions to complex 3-D problems associated with projectile and missile aerodynamics both without and with flow control.[13–16] Computational fluid dynamics (CFD) thus offers a viable approach for obtaining aerodynamics of projectiles with traditional or new flow-control mechanisms.

Recently, a number of studies, both experimental and computational, have been conducted in exploring these flow control mechanisms for projectile control. Control of a projectile has been studied using pin-based actuators at supersonic speeds by Massey and Gutrhrie[4] and flight tested.[5] This work has shown some potential of the pin-based actuators for projectile control. The control mechanism investigated in this work for projectile control is similar and consists of a set of microflaps.[6–8] In this case the flow control is achieved by locating the small microflaps between rear fins of the finned projectile. At supersonic speeds these microflaps alter the flow field in the finned region of the projectile due to shock wave interactions between the body, fins, and microflaps. These flow interactions result in asymmetric pressure distribution over the rear finned section and thus produce control forces and moments. Dykes et al.[6] used a flat-plate fin interaction design of experiments model to examine the level of control authority at Mach 1.7 and obtained an optimized layout with 4 microflaps. Sahu and Heavey[7] computationally studied the effect of microflaps on the aerodynamics of a finned

projectile using the same set of 4 flaps. Computed results indicated that the microflaps were effective at supersonic speeds and not effective at transonic speeds. The aerodynamic characterization work reported by Scheuermann et al.[8] contained both computational and flight test results. Resulting aerodynamic models were found to be in generally good agreement and continued to show promise for microflaps as a viable control mechanism at supersonic speeds ($2 < M < 3$). These previous studies using microflaps were largely based on the 4-flap configurations; the effect of the number of flaps was not investigated. Also, earlier optimization that led to the 4-flap configuration did not include the actual finned projectile geometry and was done on a flat plate.[6]

In the present study, the focus is on generation of maximum control authority on a real finned projectile configuration. A number of different geometric parameters, microflap locations, and numbers of microflaps are used to maximize the control authority generated by the flaps. In addition, the present study investigates the flow control performance of the optimized configuration at various speeds from subsonic to supersonic ($M = 0.8$ to 5.0). Computed results obtained are compared with those of the baseline configuration with 4 microflaps. In all cases, steady-state CFD is used to investigate the level of control forces and moments due to the interaction of body, fins, and microflaps flow fields.

2. Computational Methodology

The complete set of 3-D time-dependent Navier-Stokes equations is solved in a time-dependent manner for simulations of projectile flow fields. A scalable parallel Navier-Stokes flow solver, CFD++[17–19], is used, and the 3-D time-dependent Reynolds-averaged Navier-Stokes equations are solved using a finite volume method:

$$\frac{\partial}{\partial t}\int_V \mathbf{W}dV + \oint[\mathbf{F}-\mathbf{G}]\cdot dA = \int_V \mathbf{H}dV, \qquad (1)$$

where $\mathbf{W}$ is the vector of conservative variables, $\mathbf{F}$ and $\mathbf{G}$ are the inviscid and viscous flux vectors, respectively, $\mathbf{H}$ is the vector of source terms, V is the cell volume, and A is the surface area of the cell face.

Implicit local time-stepping and relaxation techniques are used to achieve faster convergence. Use of an implicit scheme circumvents the stringent stability limits encountered by their explicit counterparts, and successive relaxation allows update of cells as information becomes available and thus aids convergence. CFD++ uses an algebraic multigrid approach as the means to efficiently solve the linear algebra problem that results in applying an implicit scheme to both steady-state and

unsteady modes of operation. In the present work, only steady-state solutions have been obtained. Second-order discretization was used for flow variables and turbulent viscosity equations. Two-equation[20] k-ε turbulence models were used for computation of turbulent flows.

3.   Model Geometries and Computational Grids

The projectile modeled in this study is the Basic Finner, a cone-cylinder-finned configuration.[21] A schematic diagram of the Basic Finner shape is shown in Fig. 1. The length of the projectile is 10 cal. and the diameter is 30 mm. The conical nose is 2.84 cal. long and is followed by a 7.16-cal. cylindrical section. Four rectangular fins are located on the back end of the projectile. Each fin is 1 cal. long, has a sharp leading edge, and is 0.08 cal. thick at the trailing edge. The center of gravity is located 5.5 cal. from the nose of the finned projectile.
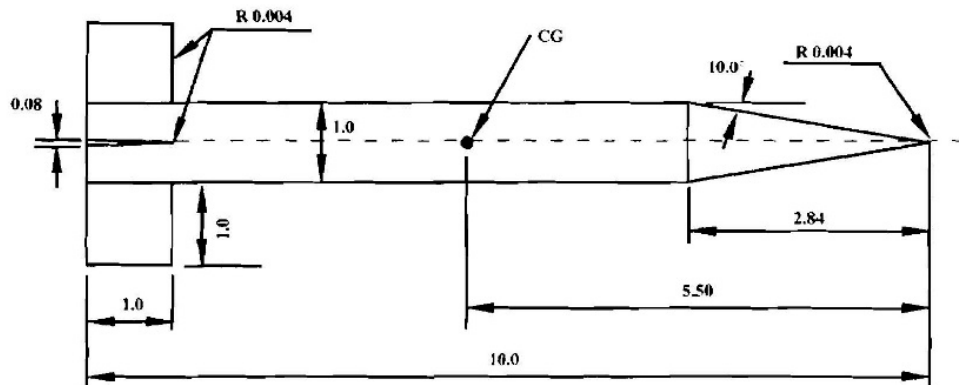
Fig. 1   Schematic of the basic finned configuration (in calibers; 1 cal. = 0.03 m)

Figure 2 shows the 3-D computational models of the finned projectile both without and with microflaps. Figure 2b shows a typical set of 6 microflaps, the control mechanisms, in this case located in 3 rows between 2 of the 4 rear fins. These microflaps, located as shown in Fig. 2, are intended to create asymmetric pressure distributions and flow fields in the aft finned section of the projectile and provide control forces and moments needed for projectile control maneuver. A number of geometric parameters as well as the number of microflaps were varied. Geometric parameters included the axial and circumferential distances or spacings between the microflaps. The circumferential distances between the microflaps were chosen by defining the angle between them. The flap thickness is about 0.512 mm and its height is 4.54 mm. Table 1 shows the geometric parameters for the 6- and 8-flap configurations. The first axial spacing is the distance between the leading edge of the fins and the first row of microflaps. The other axial spacings represent the axial distances between the front faces of the microflaps.

(a)   (b)
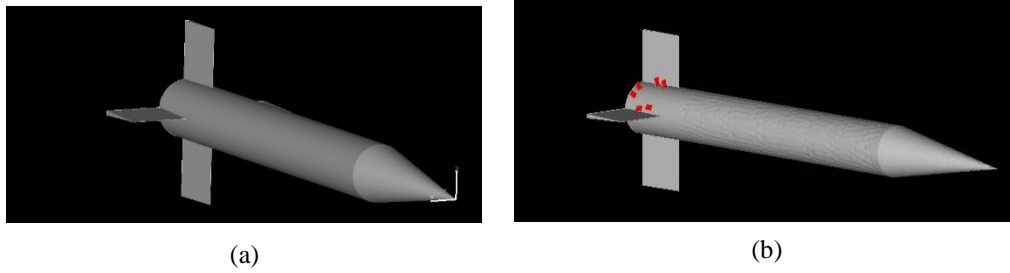
Fig. 2   Finned body geometry a) without and b) with microflap control mechanisms between 2 rear fins

Table 1   Geometric parameters used for various microflap configurations

Cases	Axial spacing (m)	Circumferential spacing in angles (°)
Case 1: 6 flaps	0.0079, 0.0079, 0.0079	60, 70, 20
Case 2: 6 flaps	0.0079, 0.0079, 0.0079	60, 40, 20
Case 3: 6 flaps	0.0079, 0.0079, 0.0079	20, 40, 60
Case 1: 8 flaps	0.006, 0.006, 0.006, 0.006	20, 35, 50, 20
Case 2: 8 flaps	0.006, 0.006, 0.006, 0.006	65, 50, 35, 20
Case 3: 8 flaps	0.006, 0.006, 0.006, 0.006	20, 35, 50, 65

Unstructured meshes were generated for all configurations without and with flaps using MIME, an unstructured mesh generator developed by Metacomp Technologies. Figure 3 shows the computational mesh for the projectile configuration without microflaps. The mesh consists of 3.4 million cells and 3.6 million nodes. Three different types of cells—tetrahedrals, triangular prisms, and pyramids—were used in the mesh. Grid points shown in Fig. 3a were clustered in the boundary layer region near the projectile body. The boundary spacing was selected to achieve a y+ value of 1.0 or less. Other regions of grid clustering included the fins and the wake regions. An expanded view of the mesh for the afterbody fin region is shown in Fig. 3b. It shows the surface mesh and the clustering used at the leading and trailing edges of the fins.

<center>(a)   (b)</center>
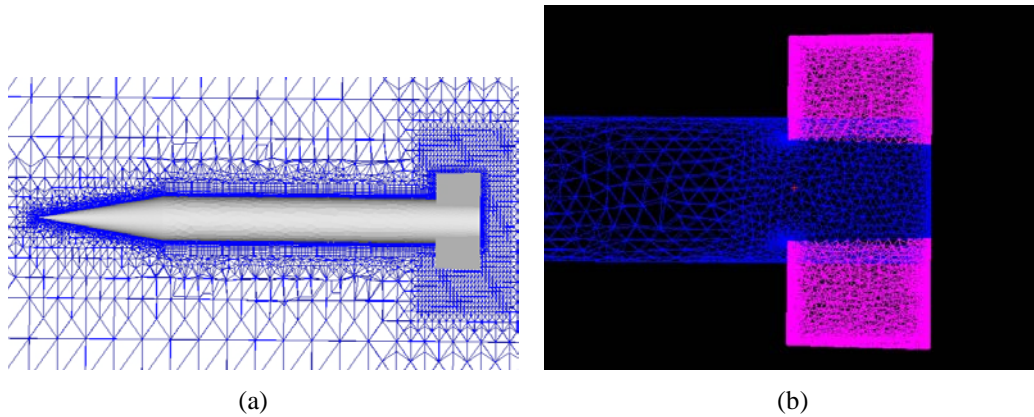
Fig. 3   **Computational grid without microflaps: a) expanded near the projectile and b) afterbody finned region**

The same unstructured technique was used to generate the meshes for the projectile configurations with the microflaps. As pointed out earlier, the microflaps were located between 2 of the 4 rear fins. Figure 4 shows the surface meshes in the afterbody fin region containing the microflaps. Figure 4a shows the meshes for the three 6-flap configurations considered, while Fig. 4b shows the same for the three 8-flap configurations. The flaps are located in 3 or 4 rows symmetrically about the z-axis; the meshes shown in Fig. 4 correspond to the xy plane. In general for the projectile configurations with microflaps, most of the grid points were clustered in the boundary layer, fins, microflaps, and wake regions. The overall unstructured meshes consist of about 4.5 million cells and 4.8 million nodes. The increased grid density for the finned body with microflaps can also be seen on the cylinder surface between the fins. The boundary spacing was selected to achieve a y+ value of 1.0, and integration of governing equations was carried out all the way to the body wall.

<p align="center">(a)   (b)</p>
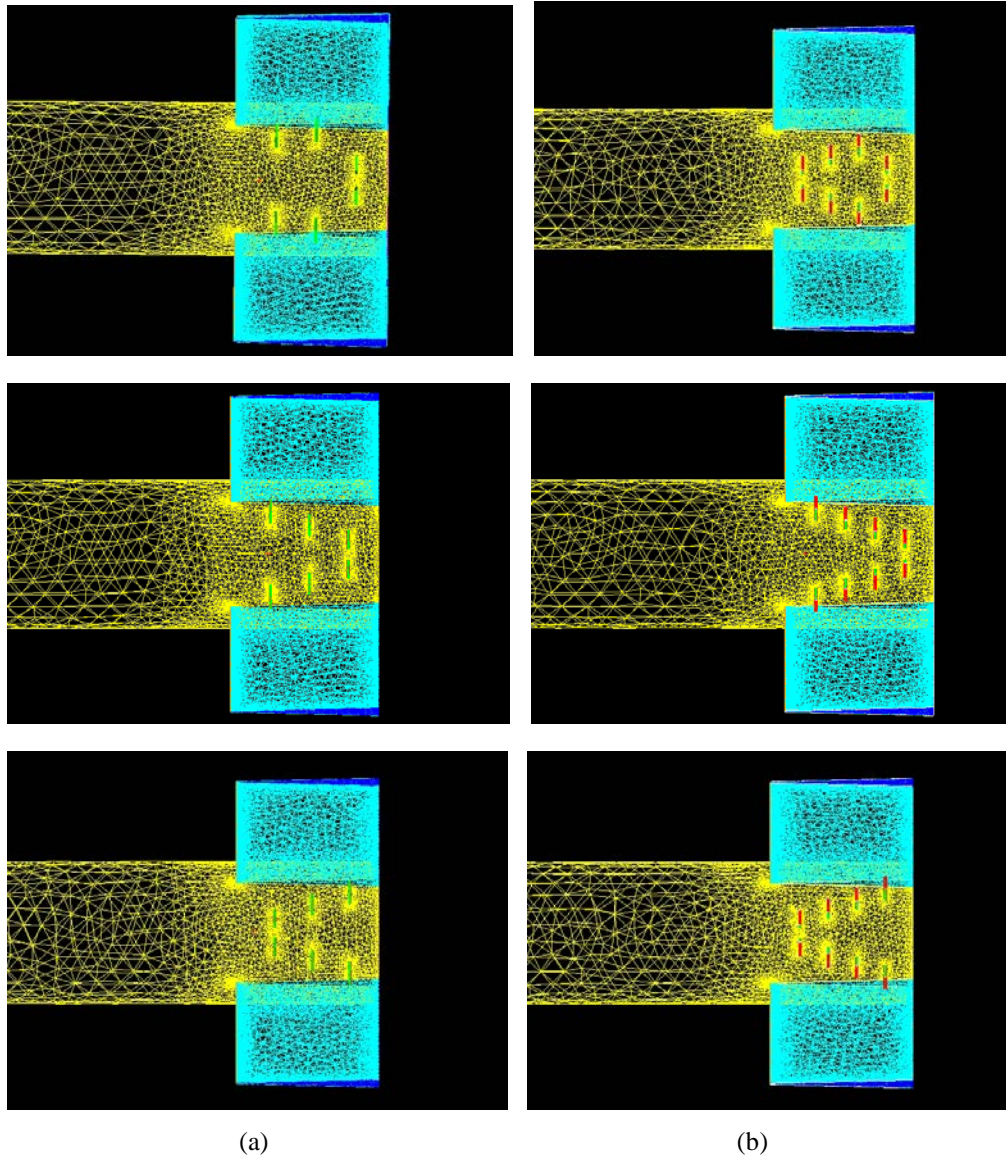
Fig. 4   Computational grids with microflaps: a) 6- and b) 8-flap cases

4.   Results

4.1 Optimization of Control Authority

Numerical simulations have been carried out at the US Air Force Defense Supercomputing Resource Center with a Cray XE-6 system using 64 processors. These computations have been performed using the advanced scalable unstructured flow solver CFD++ with a time-dependent Navier-Stokes computational technique as described earlier. In all cases, full 3-D computations using atmospheric sea level flight conditions were performed and no symmetry was used.

Steady-state computations have been performed for the finned projectile both without and with microflaps at M = 2.5 and at angle of attack α = 0°. Solutions were obtained at α = 2° for the case with no flaps. Although not shown here, computed slopes of normal force and pitching moment coefficients, $C_{N\alpha}$ and $C_{m\alpha}$, obtained for the finned projectile without microflaps were checked and found to be in very good agreement with the test data.[21,22]

For cases with flaps, computations were performed to quickly provide the extent of control forces that could be generated using the microflaps. The microflaps were pointing up in the z-direction in all these cases with the fins in the x-orientation and were located symmetrically about the z-axis. This way, no side forces were created and the control force and moment of interest were the normal force, F_z, and associated pitching moment, M_y, respectively.

Figure 5 shows the computed surface pressure contours for the finned body with the microflaps at M = 2.5 and α = 0° for the different flap cases. Computed surface contours for the three 6-flap cases are shown in Fig. 5a, while Fig. 5b shows the results for the three 8-flap cases. In Fig. 5 the flow field between the 2 fins is quite complicated when the microflaps are present. There are a lot of body, fin, and microflaps flow interactions, resulting in very complex flow fields containing multiple shocks and regions of high surface pressures. High surface pressures are shown in red and yellow, and blue represents lower pressures. As expected, the pressures in front of the flaps are high, and lower pressure regions are observed behind the flaps, especially the last row of flaps. For the 6-flap cases, the top 2 configurations seem to show similar flow structures. The third 6-flap case (bottom picture in Fig. 5a) shows much stronger shock-shock interactions, resulting in larger region of higher pressures on the fins. The same is true of the 8-flap cases, as shown in the top and bottom plots of Fig. 5b. The first 3 rows of flaps are the same between these 2 plots; the only difference is in the circumferential location of the flaps in the last row. For both the 6- and 8-flap cases, the pictures on the bottom of Fig. 5 are perhaps the best cases showing the larger regions of higher pressures than other cases.
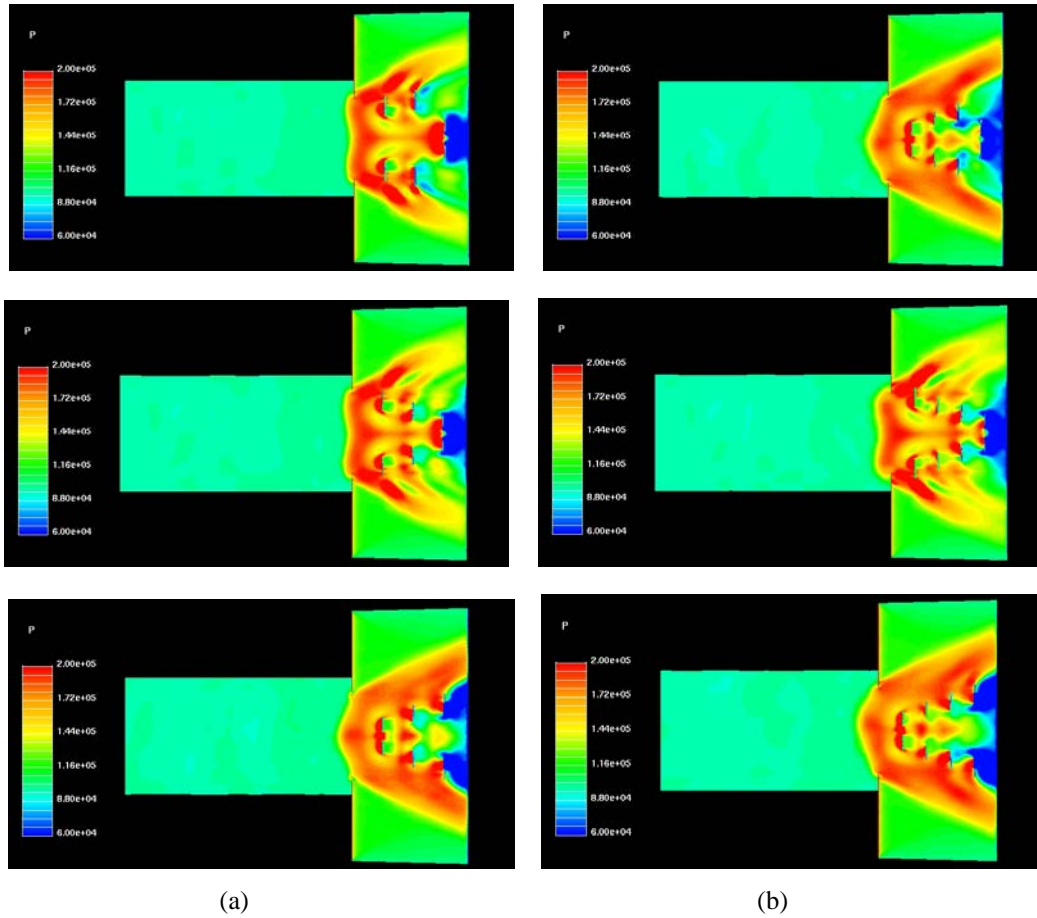
Fig. 5   Computed surface pressure contours in the afterbody fin region near the microflaps, M = 2.5, $\alpha = 0°$: a) 6- and b) 8-flap cases

As shown in Fig. 5, the strong shock interactions due to the presence of the flaps result in regions of higher pressures between the fins on the lee side (top view). On the other hand, the computed surface pressures on the afterbody between the other fins are similar to the no-flap case and show only the interaction of 2 weak shocks, and the flow field is rather a simple one (Fig. 6). The surface pressures are much lower on the wind side than the lee side where the microflaps were located. The difference in the surface pressures between the lee side and the wind side results in a negative normal force, F_z. Also, for the finned projectile without the microflaps, the normal force, as expected, is zero and so is the pitching moment at $\alpha = 0°$.
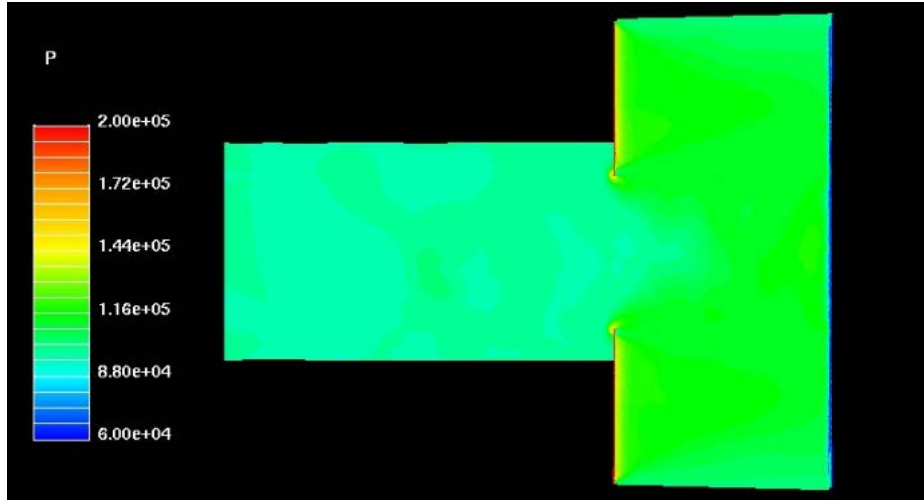
Fig. 6   Computed surface pressure contours between the fins in the wind side, M = 2.5, α = 0°

The actual change (delta) in the aerodynamic forces and moments between the Finner with microflaps and the Finner without microflaps was obtained from the computed solutions for all configurations at M = 2.5 and α = 0° and are shown in Table 2. The delta normal force and the delta pitching moment are of primary interest here. For comparison purposes, the computed result for a 4-flap configuration from Sahu and Heavey[7] is included in the first row of the table. Also included in the last row of the table is the result obtained for a 1-flap configuration (Fig. 7). One flap alone produces 11 N of control force and a pitching moment of 1.5 N-m. The flap was not perfectly placed symmetrically in this case and thus the flow field does show some asymmetry. The remaining cases include three 6-flap and three 8-flap configurations. As shown in Table 2, all 6 of these flap configurations produce normal force in the range of 47–56 N compared with 40 N obtained with a 4-flap configuration. It seems the larger the number of flaps, the larger the control normal force and pitching moment, especially with the 6-flap configurations. However, the net gain in control force and moment in going from 6 to 8 flaps is smaller than that achieved in going from 4 to 6 flaps. As explained earlier in Fig. 5, case 3 from the 6-flap arrangement and case 3 from the 8-flap arrangement show larger regions of high pressures especially on the fins and are perhaps the best cases that produce the most control force and moment. Since the microflaps were located symmetrically with respect to the z-axis, the Fy force and the moments, Mx and Mz, are zero and so are the deltas in those force and moments. Note the drag penalty that results from the presence of microflaps. The increase in drag for all 6- and 8-flap configurations is also included in the table and is generally in the same range. One can thus maximize the control normal force and pitching moment to obtain the best configuration possible.

Table 2 Delta forces and moments due to microflaps, M = 2.5, α = 0°

Case	Delta normal force δF_z (N)	Delta pitching moment δM_y (N-m)	Delta axial force (N)
4 flaps [ref. 7]	–40.0	4.20	17.0
Case 1: 6 flaps	–47.5	5.87	19.9
Case 2: 6 flaps	–50.2	6.23	20.0
Case 3: 6 flaps	–50.8	6.34	21.2
Case 1: 8 flaps	–51.4	6.25	20.2
Case 2: 8 flaps	–52.5	6.34	21.6
Case 3: 8 flaps	–55.5	6.80	23.1
1-flap case	–11.0	1.50	6.0

a
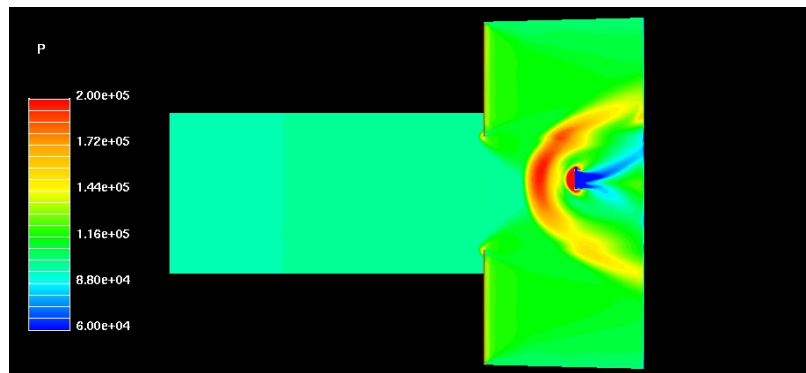
Fig. 7   Computed surface pressure contours in the afterbody fin region near the microflap for a 1-flap case, M = 2.5, α = 0°

As discussed earlier, case 3 from the 6- and 8-flap configurations (Table 1 and Fig. 5) seemed to be the best cases for control force and moment. In the results in Fig. 5, especially the bottom row pictures, there are large regions of lower pressures shown in blue. If these regions of lower surface pressures could be eliminated or at least reduced, it could possibly lead to overall higher surface pressures in the whole region containing the microflaps and, ultimately, larger control force and moment. One idea to achieve this was to change the axial distances between the different rows of microflaps such that the last row of microflaps sat right at the end of the projectile flush with the base (Fig. 8). The actual axial distances are shown in Table 3 as case 4 for both new 6- and 8-flap configurations. Table 3 also includes case 3

for comparison purposes. Compared with case 3 for the 6- and 8-flap configurations, where the rows of flaps were equally spaced between the leading edge and the trailing edge of the fins, the first axial spacing between the leading edge of the fins and the first rows of flaps was first set to 0.006 m and then increased for the remaining rows to push the last row to the trailing edge of the fins or the end of projectile. This was done in an attempt to maximize the surface pressures both ahead of the first row of flaps and to eliminate the lower pressure region behind the last row of flaps seen previously. The circumferential spacings for both of these new cases were kept unchanged from the case 3 of both 6-flap configurations and the 8-flap configuration.

(a) (b)
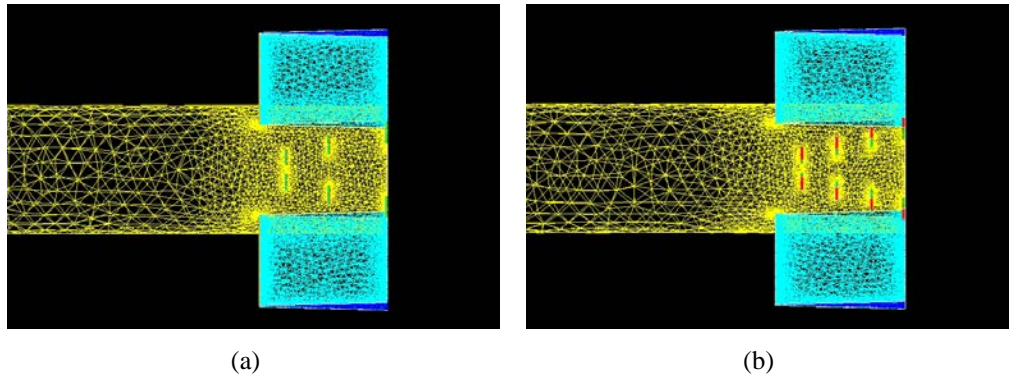
Fig. 8 Computational grids for the new microflap cases: a) 6 and b) 8 flaps

Table 3 New geometric parameters used for 2-microflap configurations (case 4)

Case	Axial spacing (m)	Circumferential spacing in angles (°)
Case 3: 6 flaps	0.0079, 0.0079, 0.0079	20, 40, 60
Case 4: 6 flaps	0.006, 0.01, 0.01349	20, 40, 60
Case 3: 8 flaps	0.006, 0.006, 0.006, 0.006	20, 35, 50, 65
Case 4: 8 flaps	0.006, 0.008, 0.008, 0.00749	20, 35, 50, 65

Computed surface pressure contours for the 2 new 6- and 8-flap configurations are shown in Fig. 9a and Fig. 9b, respectively. These results, shown as case 4 and case 3 results, are included here for direct comparison with case 4 results. In Fig. 9 the lower-pressure regions shown in blue, with case 3 having largely been eliminated with the new 6- and 8-flap configurations. There is a small region of lower pressures behind the second row of flaps in the 6-flap configuration, but overall the surface pressures downstream are much larger for case 4. These larger surface pressures clearly lead to larger control force and moment for the new 6- and 8-flap

configurations (Table 4). As seen in Table 4, case 4 now represents even better candidates for maximum control authority with approximately 5 N of additional control force achieved compared with case 3 without adding any significant additional drag penalty.

(a) Case 3   (b) Case 3

(a) Case 4   (b) Case 4
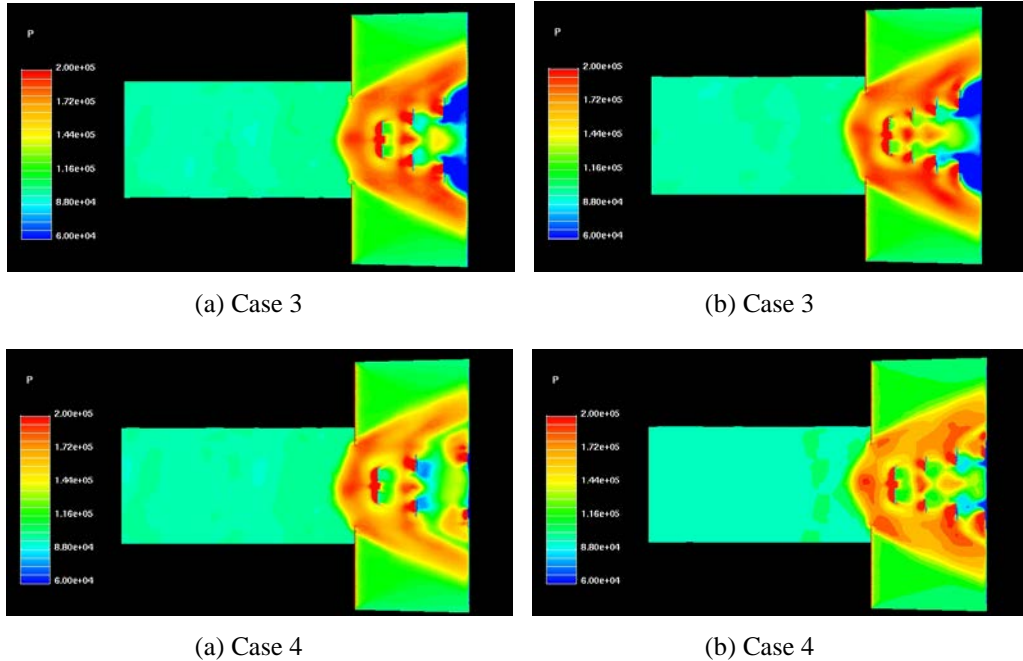
Fig. 9   Computed surface pressure contours in the afterbody fin region near the microflaps, case 3 vs. case 4, M = 2.5, $\alpha = 0°$: a) 6- and b) 8-flap cases

Table 4   Comparison of delta forces and moments, case 3 vs. case 4, M = 2.5, $\alpha = 0°$

Case	Delta normal force δF_z (N)	Delta pitching moment δM_y (N-m)	Delta axial force (N)
Case 3: 6 flaps	−50.8	6.34	21.2
Case 4: 6 flaps	−55.2	6.93	21.6
Case 3: 8 flaps	−55.5	6.80	23.1
Case 4: 8 flaps	−60.6	7.56	23.7

4.2 Effect of Flap Height

A few cases have been run in an attempt to quantify the effect of changing microflap heights, in particular staggering the heights from low in the first row of flaps to high in the last row. Again, both 6-flap configurations and the 8-flap configurations were considered. For each configuration, the heights were changed linearly from h to 2h for case 5 and 0.5 h to h for case 6. Here, h is the original height used in cases 1–4. Computed surface pressure contours for the 2 new 6-flap and 2 new 8-flap configurations are shown in Fig. 10a and Fig. 10b, respectively. In case 5, the increase in height for the flaps from h to 2h, as expected, created a lot more interactions and increase in surface pressures in the whole region and especially on the fins containing the flaps. On the other hand, in case 6, decreasing the heights from h in the back row to 0.5 h in the front basically reduced the interaction region, leading to lot lower surface pressures in this region compared with case 5.

(a) Case 5   (b) Case 5

(a) Case 6   (b) Case 6
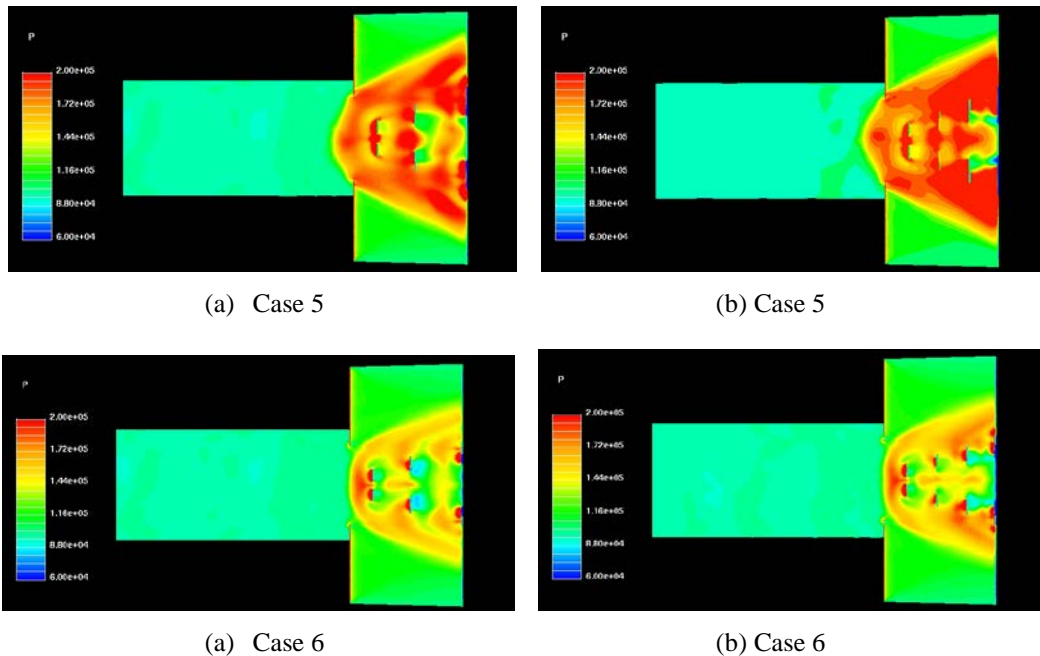
Fig. 10   Computed surface pressure contours in the afterbody fin region near the microflaps, flap height variation, M = 2.5, α = 0°: a) 6- and b) 8-flap cases

The resultant control forces and moments are shown in Table 5 for the cases with changing flap heights. Clearly, reducing the heights from the original one in case 6 produces similar or less control force than the baseline case, but the drag penalty is a little less, true for both 6- and 8-flap configurations. The best case seems to be case 5, where the heights were increased from h in the first row to 2 h in the last row of flaps. A very large control force and, correspondingly, a large control moment are obtained for both 6- and 8-flap configurations; however, associated with large control force and moment is also a large, undesirable increase in drag.

Table 5   Comparison of delta forces and moments, case 5 vs. case 6, M = 2.5, α = 0°

Case	Delta normal force δF_z (N)	Delta pitching moment δM_y (N-m)	Delta axial force (N)
Case 5: 6 flaps	–83.0	10.84	42.4
Case 5: 8 flaps	–97.2	12.57	46.1
Case 6: 6 flaps	–36.3	4.66	13.2
Case 6: 8 flaps	–40.9	5.21	14.6

4.3 Effect of Angle of Attack

All the results presented here for different angles of attack are again at the same Mach number, M =2.5. Again the effect of angle of attack is studied using one of the best candidate configurations, case 4 with 8 flaps. Computed results have been obtained for this 8-flap configuration at various angles of attack from –16° to 16°. The resultant delta control forces and moments are shown in Table 6. These results seem to indicate that control force and moment are generated across the range of angle of attack considered here. Also, the variation with angle of attack is not as significant for positive angles of attack; however, for negative angles of attack, the deltas in control forces and moment gets larger with increase in angles of attack.

Table 6   Variation of delta forces and moments due to microflaps with angle of attack, M = 2.5

Angle of attack α (°)	Delta normal force δF_z (N)	Delta pitching moment δM_y (N-m)	Delta axial force (N)
–16	–100	13.19	49.1
–12	–91.7	11.96	43.9
–8	–91.7	11.91	39.7
–4	–81.6	10.49	33.7
–2	–72.0	9.19	28.7
0	–61.6	7.74	23.4
2	–52.5	6.48	19.2
4	–45.7	5.56	16.7
8	–44.5	5.29	16.0
12	–57.4	6.85	18.3
16	–64.0	7.51	19.2

4.4 Effect of Mach Number

All the results presented so far have been at one Mach number, M = 2.5. Of critical importance is the flow control performance of the microflaps at other speeds (transonic and subsonic) as well. Here the effect of Mach number is studied using the optimized 8-flap configuration (case 4). Computed results have been obtained for this 8-flap configuration at various speeds from M = 0.8 to 5.0.

Computed surface pressures in the afterbody region near the microflaps are shown in Fig. 11 at different Mach numbers and $\alpha = 0°$. As shown, the higher the Mach number, the larger is the extent of flow interactions. At supersonic speeds, one can see shock interactions and a complex shock structure in the afterbody region containing the flaps. With increasing speed in the supersonic regime, the shock interactions become stronger, resulting in much higher surface pressures near the flaps and on the 2 fins containing the flaps.
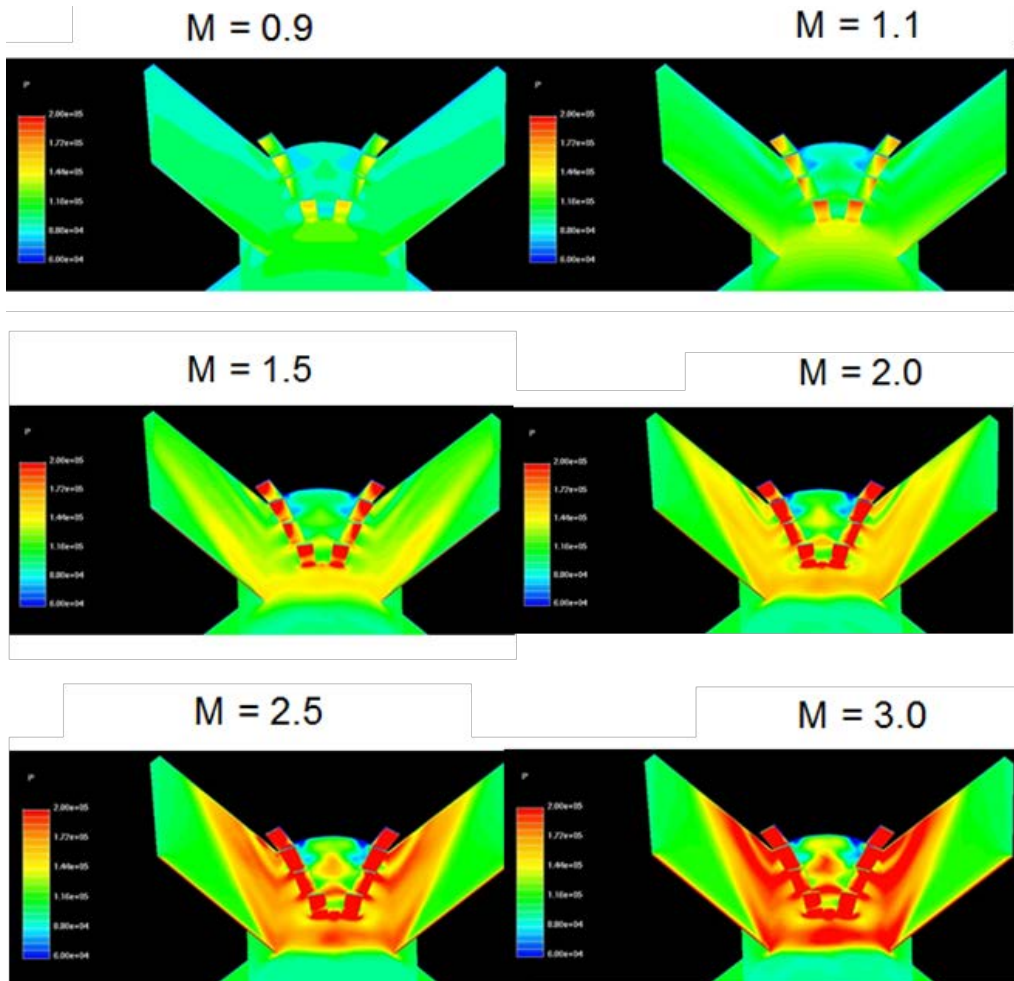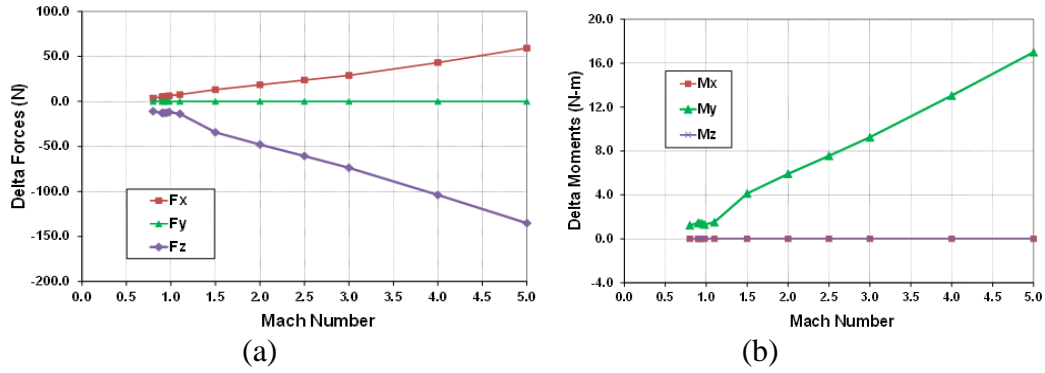

Fig. 11   Computed surface pressure contours in the afterbody fin region near the microflaps for the 8-flap optimized configuration at various Mach numbers, $\alpha = 0°$

15

The resultant delta control forces and moments are shown in Table 7. These results seem to indicate that control force and moment are generated across the Mach number range considered. Also, the higher the Mach number, the larger are the delta control forces and the moment for supersonic speeds, M > 1.5. It is interesting that control force and moment are generated at subsonic speed, M = 0.8, as well as across the transonic speed regime, 0.9 < M < 1.1, and they are almost constant in this speed regime. It is clear that potential exists for these microflaps to provide some control authority at all speeds including subsonic and transonic. Computed results for this optimized 8-flap configuration is compared with the 4-flap baseline configuration (Figs. 12 and 13). With only a slight penalty in drag, substantially larger control force and moment are obtained for the 8-flap configuration. Also, note that microflaps are not effective with the baseline configuration at M = 1.2 or less, whereas the new 8-flap configuration is still effective at M = 1.1 and below at subsonic and transonic speeds.

Table 7   Variation of delta forces and moments due to microflaps with Mach number, $\alpha = 0°$

Mach no.	Delta normal force δF_z, (N)	Delta pitching moment δM_y, (N-m)	Delta axial force (N)
0.80	−10.9	1.23	3.7
0.90	−12.8	1.44	5.1
0.92	−12.8	1.44	5.4
0.95	−12.6	1.4	5.8
0.98	−11.8	1.3	6.3
1.1	−13.7	1.51	7.7
1.5	−34.4	4.13	13.1
2.0	−47.8	5.92	18.5
2.5	−60.6	7.56	23.7
3.0	−73.7	9.25	29.0
4.0	−103.9	13.05	43.1
5.0	−135.2	17.00	59.2

Fig. 12   Variation of delta aerodynamic forces and moments due to microflaps as a function of Mach number for the 8-flap optimized configuration, $\alpha = 0°$: a) delta forces and b) delta moments
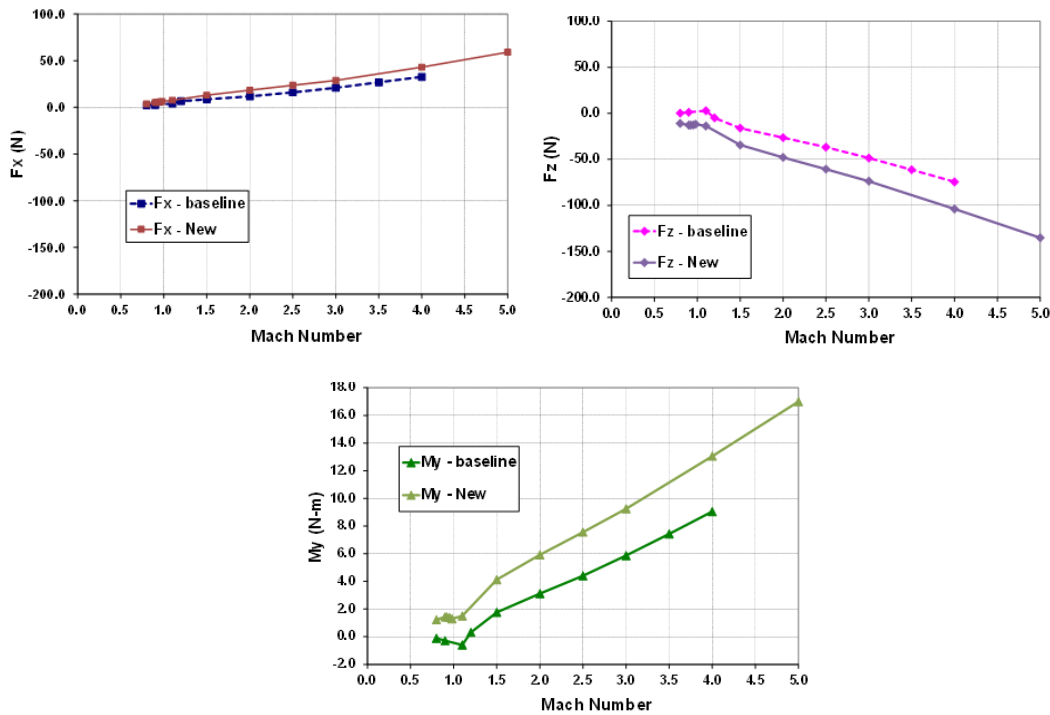
Fig. 13   Comparison of delta forces and moment between the baseline and the optimized 8-flap configurations, $\alpha = 0°$: (top left) delta axial force, (top right) delta normal force, and (bottom) delta pitching moment

4.5 Flight Dynamic Simulations

These changes in the aerodynamic force and moments due to presence of microflaps can be used in 6 degrees of freedom (6DOF) flight dynamic simulations to examine the feasibility of microflaps as control mechanism to provide adequate control authority for projectile control. For practical applications, the microflaps will need to go in and out as the body rolls depending on the control maneuver. For

example, if a cross-range maneuver is needed, the microflaps can be actuated in the y-direction for part of the roll cycle (off for the remainder of the roll cycle) so control forces are generated in that direction and are used for control of the projectile. Flight dynamic trajectory simulations of a representative cross-range control maneuver were performed using the "boom" 6-DOF body dynamics code developed by Costello.[23] Results obtained from these simulations show the effectiveness of microflaps in terms of the cross-range or deflection of the finned projectile (Fig. 14), which shows both uncontrolled and controlled trajectories. Compared with the baseline configuration, the new optimized 8-flap configuration results in 60% more control in the cross range.
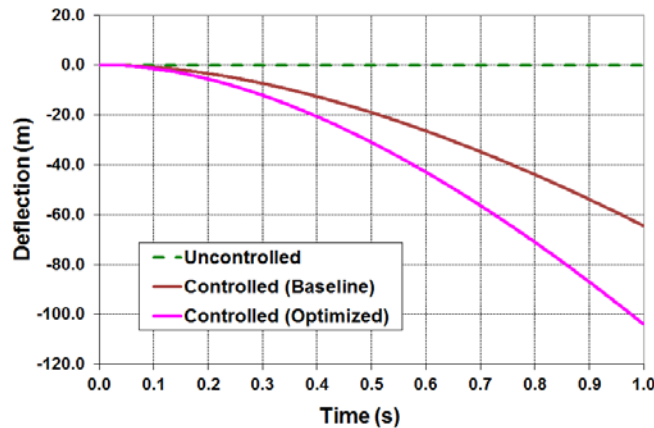

Fig. 14   Flight dynamic results showing trajectory deflection control due to microflaps; initial M = 2.5

4.6 Flow Control Effect with Fins Removed

Here the effect of Mach number is studied using the same optimized 8-flap configuration (case 4). This time fins have been removed from the body. Of interest is the control force that would be generated on the body by the flaps for the body with no fins. Again, computed results have been obtained for the optimized 8-flap configuration at various speeds from M = 0.8–5.0. Computed results (delta forces and delta moment) are shown in Table 8 and in Fig. 15. For 0° angle of attack, delta normal force is same as the actual normal force, and the same is true for the delta pitching moment. The delta axial force is the difference between the axial force with flaps and without flaps (body only). These results clearly show that control force and moment generated by the flaps are diminished by about half at supersonic speeds and a little more at lower speeds when fins are removed. Also, the flaps are found to be ineffective at subsonic and transonic Mach numbers of Mach 1.2 or less for the no-fin case. Although not shown here, results for the 8-flap no-fin case are similar to the 4-flap baseline case.

Table 8   Delta forces and moments due to microflaps, no fins, $\alpha = 0°$

Mach no.	Delta normal force δF_z (N)	Delta pitching moment δM_y (N-m)	Delta axial force (N)
0.80	–2.19	0.23	1.5
0.90	–2.74	0.30	2.4
0.92	–2.90	0.31	2.6
0.95	–2.94	0.32	3.0
0.98	–2.74	0.30	3.6
1.1	–2.89	0.33	4.7
1.5	–9.11	1.14	8.5
2.0	–16.53	2.12	14.1
2.5	–24.32	3.13	19.9
3.0	–32.53	4.20	23.7
4.0	–50.92	6.56	37.9
5.0	–71.27	9.18	52.8

(a)   (b)
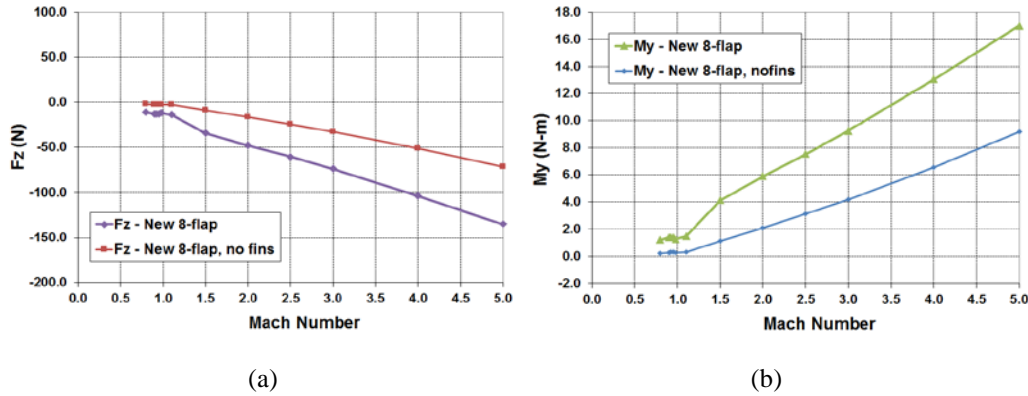
Fig. 15   Variation of delta aerodynamic forces and moments due to microflaps as a function of Mach number, $\alpha = 0°$, no fins: a) delta force F_z and b) delta moment M_y

5.   Conclusions

This report describes a computational study undertaken to determine the free-flight aerodynamics of a finned projectile with flow control. The microflaps located between the rear fins of the projectile serve as the control mechanism for flow control. Advanced Navier-Stokes CFD techniques were used to compute the aerodynamics and the interaction effects associated with the microflap control mechanism.

Steady-state Navier-Stokes solutions were first obtained for the finned projectile both without and with microflaps at a supersonic velocity, M = 2.5. Computed results for the configurations with the microflaps were first obtained at 0° angle of attack. Different geometric parameters (i.e., flap locations, distance between the

flaps, and the number of flaps) were varied to maximize the control authority. Control forces and moments were generated at this supersonic speed due to fin body–microflaps shock interactions resulting in higher pressures in the fin/body region containing the microflaps. Computed results obtained with the new 6- and 8-flap configurations produced larger control normal forces up to 21 N more than that produced by the baseline 4-flap configuration. Similar results were also obtained for the control pitching moment due to the microflaps. Computations were performed at this Mach for a range of angles of attack and control forces, and moments were also generated across the range of angle of attack considered.

An optimized 8-flap configuration was then selected and investigated for a range of Mach numbers from M = 0.8 to 5. These results show larger control forces and moments with increasing Mach number indicating that microflaps would be effective across these speeds with the new 8-flap configuration. This new configuration also produced substantially larger control force and moment than the baseline 4-flap configuration. The results also show that some control effectiveness of the microflaps exists even at transonic and subsonic speeds where the baseline 4-flap configuration failed.

The control force and moment generated by the microflaps were also used in a 6DOF flight dynamic analysis for cross-range control of the finned projectile. Flight dynamic trajectory simulations clearly show 60% more control authority in cross-range with the new optimized 8-flap configuration than the baseline 4-flap configuration.

This report has demonstrated the use of an advanced CFD technique to rapidly determine and maximize the control authority for a finned projectile with microflaps. More-sophisticated multidisciplinary design and optimization techniques can certainly be used, but it is presumed that the net gain by this process may not be worth the extra time and effort. Additional research may be needed to include any unsteady effects that result from the actual deployment of microflaps. Time-accurate advanced CFD and coupled CFD/RBD (rigid body dynamic)[24,25] techniques can also be used in future to provide detailed understanding of the unsteady aerodynamics processes involving flow control mechanisms for advanced maneuvering munitions.

6.   References

1. Sahu J. Unsteady numerical simulations of subsonic flow over a projectile with jet interaction. Presented at the 41st Aerospace Sciences Meeting; 2003 Jan 6–9; Reno, NV. AIAA Paper No.: 2003-1352.

2. DeSpirito J. Transient lateral jet interaction effects on a generic fin-stabilized projectile. Presented at the 30th AIAA Applied Aerodynamics Conference; 2012 June; New Orleans, LA. AIAA Paper No.: 2012-2907.

3. Sahu J. Unsteady aerodynamic simulations of a canard-controlled projectile at low transonic speeds. Presented at the AIAA Atmospheric Flight Mechanics Meeting; 2011 Aug; Portland, OR. AIAA Paper No.: 2011-6336.

4. Massey KC, Guthrie KB. Optimized guidance of a supersonic projectile using pin-based actuators. Presented at the Applied Aerodynamics Conference; 2005 June; Toronto, Canada. AIAA Paper No.: 2005-4966.

5. Massey KC, Silton SI. Testing the maneuvering performance of a Mach 4 projectile. Presented at the AIAA Applied Aerodynamics Conference; 2006 June; San Francisco, CA. AIAA Paper No.: 2006-3649.

6. Dykes J, Costello M, Cler DL, Carson R, Dillon R. Use of micro spoilers for control of finned projectiles. Presented at the AIAA Atmospheric Flight Mechanics Conference; 2010 Aug 2–5; Toronto, Canada.

7. Sahu J, Heavey KR. Parallel CFD computations of projectile aerodynamics with a flow control mechanism. Computers and Fluids. 2013;88(1):678–687.

8. Scheuermann E, Costello M, Silton S, Sahu J. Aerodynamic characterization of a microspoiler system for supersonic projectiles. AIAA Journal of Spacecraft and Rockets. 2015;52(1):253–263.

9. Smith BL, Glezer A. The formation and evolution of synthetic jets. Journal of Physics of Fluids. 1998;10(9):2281–2297.

10. Amitay M, Kibens V, Parekh D, Glezer A. The dynamics of flow reattachment over a thick airfoil controlled by synthetic jet actuators. AIAA Paper No. 99-1001; 1999.

11. He Y, Kral L. Post-stall control on an airfoil using localized jet actuators. AIAA Paper No.: 2000-0408; 2000.

12. Sahu J, Heavey KR. Unsteady CFD modeling of micro-adaptive flow control for an axisymmetric body. International Journal of Computational Fluid Dynamics. 2006;5:25.

13. Silton S. Navier-Stokes computations for a spinning projectile from subsonic to supersonic speeds. Journal of Spacecraft and Rockets. 2005;42(2):223–231.

14. Bhagwandin V, Sahu J. Numerical prediction of pitch damping derivatives for a finned projectile at angles of attack. Presented at the 50th AIAA Aerospace Sciences Meeting; 2012 Jan; Nashville, TN. AIAA Paper No.: AIAA-2012-691.

15. Sahu J. Time-accurate computations of free-flight aerodynamics of a spinning projectile with and without flow control. Aberdeen Proving Ground (MD): Army Research Laboratory (US); 2006 Sep. Report No.: ARL-TR-3919.

16. Sahu J, Costello M, Montalvo C. Development and application of multidisciplinary computational techniques for projectile aerodynamics. Presented at the 7th International Conference on Computational Fluid Dynamics; 2012 July; Big Island, HI. Paper No.: ICCFD7-4504.

17. Peroomian O, Chakravarthy S. A grid-transparent methodology for CFD. AIAA Paper 97-0724;1997.

18. Batten P, Goldberg U, Chakravarthy S. Sub-grid turbulence modeling for unsteady flow with acoustic resonance. Presented at the 38th AIAA Aerospace Sciences Meeting; 2000 Jan; Reno, NV. AIAA Paper No.: 2000-0473

19. Peroomian O, Chakravarthy S, Palaniswamy S, Goldberg U. Convergence acceleration for unified-grid formulation using preconditioned implicit relaxation. AIAA Paper No.: 98-0116; 1998.

20. Goldberg U, Peroomian O, Chakravarthy S. A wall-distance-free K-E model with enhanced near-wall treatment. ASME Journal of Fluids Engineering. 1998;120:457–462.

21. Dupuis A, Hathaway W. Aeroballistic range tests of the basic finner reference projectile at supersonic velocities. Valcartier (Cananda): Defence Research Establishment Valcartier; 1997 Aug. Report No.: DREV-TM-9703.

22. Dupuis A. Aeroballistic range and wind tunnel tests of the basic finner reference projectile from subsonic to high supersonic velocities. Valcartier (Cananda): Defence Research and Development Canada Valcartier; 2002 Oct. Report No.: TM-2002-136.

23. Costello M. Extended range of a gun launched smart projectile using controllable canards. Shock and Vibration. 2001;8(3–4):203–213.

24. Sahu J. Time-accurate numerical prediction of free-flight aerodynamics of a finned projectile. AIAA Journal of Spacecraft and Rockets. 2008;45(5):946–954.

25. Sahu J. Virtual fly-out simulations of a spinning projectile from subsonic to supersonic speeds. Presented at the 29th AIAA Applied Aerodynamics Meeting; 2011 June; Honolulu, HI. AIAA Paper No.: 2011-3026.

1 (PDF)	DEFENSE TECHNICAL INFORMATION CTR DTIC OCA
2 (PDF)	DIRECTOR US ARMY RESEARCH LAB RDRL CIO LL IMAL HRA MAIL & RECORDS MGMT
1 (PDF)	GOVT PRINTG OFC A MALHOTRA
1 (PDF)	DIR USARL RDRL WML E J SAHU